The effect of remote sensing resolution limits on aeolian sandstone measurements and the reconstruction of ancient dune fields on Mars: Numerical experiment using the Page Sandstone, Earth

Benjamin T. Cardenas*[1,2], Travis Swanson[3], Timothy A. Goudge[1], R. Wayne Wagner[4], and David Mohrig[1]

[1]Jackson School of Geosciences, University of Texas at Austin, Austin, Texas, USA

[2]now at Division of Geological and Planetary Sciences, California Institute of Technology, Pasadena, California, USA

*Corresponding Author Contact Information

Email: bencard@caltech.edu

In review at Journal of Geophysical Research: Planets

THIS IS A NON-PEER REVIEWED PRE-PRINT SUBMITTED TO EARTHARXIV AND UNDER REVIEW AT THE JOURNAL OF GEOPHYSICAL RESEARCH: PLANETS

Pages: 34

Figures: 8

References: 49

KEY POINTS

Field-gathered aeolian cross-set thicknesses are altered to mimic measurement error from remote sensing pixel resolution limits.

Remote sensing resolution limits can severely alter interpretations of aeolian sandstones, even at HiRISE resolution.

Accurate measurements require outcrop slopes less than 13° steep, such that the thinnest sets are exposed over detectable distances.

PLAIN LANGUAGE SUMMARY

The thickness of wind-blow sand dune deposits are called cross sets. Cross sets can be preserved for long amounts of time as sedimentary rocks, where they act as a record of the ancient surface. A collection of many cross-set thickness measurements can be organized into a distribution of thinner and thicker sets with a particular shape. The shape of the distribution can be analyzed to understand the motion of ancient sand dunes, and in turn the conditions of ancient planetary surfaces. On Earth, we can measure cross-set thicknesses in the field and collect accurate measurements, but for Mars we are mostly limited to satellite images. Here, we perform a numerical experiment on Earth-collected cross-sets from the Page Sandstone. The experiment mimics alters the Earth measurements to become less accurate, as if detected from satellite. The altered distribution is checked for changes which might affect our understanding of the ancient dune fields. Our results show that there is a significant risk of misinterpretation, but that good measurements can be made if the slope of the rock outcrop is shallow, less than 13° from horizontal, such that the thinnest cross sets are exposed over long distances, making them detectable from satellite.

ABSTRACT

The distribution of cross-set thicknesses is important field-collected data for reconstructing ancient aeolian dune fields from the strata they accumulated, but most aeolian strata on Mars must be observed with remote sensing. We hypothesize that remote sensing resolution limits will affect cross-set thickness measurements and the dune field reconstructions that follow. Here, we test this hypothesis using a numerical experiment mimicking the effects of remote sensing resolution limits performed on a distribution of aeolian cross-set thicknesses measured in the field from the Page Sandstone, Arizona, USA. Page set thicknesses are exponentially distributed, representing the accumulations of dry (no water table) dune fields in a state of net-sediment bypass. Set-thickness measurements are progressively blended into adjacent sets based on the map-view distance between their upper and lower bounding surfaces on exposures with different dips. This is termed the “exposure distance” of a cross set, and in this experiment is a function of (1) set thickness, (2) the dip of the outcrop surface, and (3) assumptions of the number of remote sensing image pixels required to detect a set (detection limit). Using outcrop dips from 1° to 60° and detection limits from 3 to 10 HiRISE pixels, gently sloping surfaces (< 13°) allow most of the Page Sandstone sets to be measured, conserving the bypass interpretation made from the true set thicknesses at all detection limits. Although these results are specific to the Page, they can be used as a rule of thumb for future Mars work.

1. INTRODUCTION

The distribution of aeolian cross-set thickness is among the easiest stratigraphic data to collect, and the shape of the distribution, as well as its statistical moments, records the aggradation, migration, and the size of dunes in a field (Cardenas et al., 2019; Swanson et al., 2019). Wind is the dominant driver of sediment transport on modern Mars (Ewing et al., 2010; Fenton and Haywall, 2010; Silvestro et al., 2011; Silvestro et al., 2013; Chojnacki et al., 2015; Day and Kocurek, 2016; Lapotre et al., 2016; Cornwall et al., 2018a and b; Chojnacki et al., 2019) and likely been significant throughout the planet's history (e.g., Grotzinger et al., 2005; Lewis et al., 2008a and b; Kite et al., 2013; Milliken et al., 2014; Banham et al., 2018; Anderson et al., 2018; Day and Catling, 2018 and 2019). Even on Earth, where a more diverse set of processes have shaped the planet's surface, the aeolian rock record dates back at least as far as the Archean (3.2 Ga; Rodríguez-López et al., 2014). Therefore, aeolian strata are likely to provide a rich source of information about autogenic processes and paleo-environmental boundary conditions at the ancient surface of Mars, as martian bedform dynamics are controlled by environmental conditions and autogenic processes. Measuring set thicknesses of aeolian sandstones on Mars has the potential to increase our understanding of these ancient conditions on Mars through time. Cross-set thicknesses are observable from remote sensing images and digital elevation models (DEMs; e.g., Milliken et al., 2014; Anderson et al., 2018; Day and Catling, 2019). However, resolution limits may lead to remotely-measured thickness distributions that are not representative of the true distribution. This may, in turn, lead to mis-interpretations of the stratigraphy and the ancient martian surface environment. The best currently-available remote sensing images and stereo-derived DEMs of Mars come from the High Resolution Imaging Science Experiment (HiRISE) camera, and have a spatial resolution of 0.25 m/pixel (images) and 1 m/pixel (DEMs) (McEwen et al., 2007; Kirk et al., 2008). However, this is still coarse relative to field observations. We hypothesize that this resolution limit has an effect on measurements of set thicknesses and the dune field reconstructions based on them.

Here, we perform a numerical experiment using a field-acquired distribution of aeolian cross-set thicknesses from the middle Page Sandstone, Arizona, USA (Cardenas et al., 2019). In this experiment, the population of cross-set thicknesses is modified through the blending of thinner sets into thicker sets on the basis of outcrop dip, the size of a remote sensing image pixel, and the number of pixels needed to identify a unique set of cross strata. The aim is to blend thinner, undetected sets into thicker sets, such that the original dataset is altered in a way that mimics the sub-pixel mixing of a remote sensing image. The ancient environment recorded by the Page Sandstone and its dynamics are well studied (Cardenas et al., 2019; Swanson et al., 2019), and we compare these to re-interpretations of the ancient dune field based on the experimental, resolution-filtered distributions. The distributions are compared using statistical moments (mean, standard deviation, and products thereof), distribution shapes, and the number of measurements remaining in a filtered dataset. The goal of this contribution is to enable quantitative measurements of aeolian strata on Mars that take appropriate caution during interpretation, and providing guidance on minimizing this potential source of error.

1.1 Reconstruction of dune-field kinematics from cross-set-thickness distributions

In aeolian dune fields, the controls on dune aggradation are important representations of surface conditions. These autogenic processes include dune interactions (Ewing and Kocurek, 2010a and b; Day and Kocurek, 2018) and natural variation in dune scour depths (Paola and Borgman, 1991; Jerolmack and Mohrig, 2005; Cardenas et al., 2019; Swanson et al., 2019). Environmental boundary conditions include wind regime, sediment availability and source geometry, basin geometry, the proximity of the water table to the surface, and antecedent topography (Kocurek et al., 2010; Ewing et al., 2015; Chojnacki et al., 2019; Cardenas et al., 2019; Swanson et al., 2019).

Bypassing dune fields are able to accumulate and preserve cross sets via the filling of their own variably deep dune trough scours that form as the dunes migrate, without the need for net-bed aggradation (Paola and Borgman, 1991). These cross sets are laterally discontinuous, as they primarily represent the fill of the deepest local scours. This favors the preservation of thin, heavily scoured sets and thick, scour-filling sets. As such, the variability in set thickness is greater than the variability in dune scour depths. In contrast, laterally continuous, climbing cross sets record steady bed aggradation and will not favor the preservation of cross sets filling the deepest scours as strongly, meaning a greater percentage of dunes have preserved cross sets (Allen, 1973; Rubin and Hunter, 1982; Bridge and Best, 1997; Leclair et al., 1997; Jerolmack and Mohrig, 2005; Swanson, 2019). As a result, the variability in cross-set thickness is closer to the variability in dune scour depths.

To better understand the relative contributions of scour depth and bed aggradation, and therefore the forcings upon the dune field, the distribution of cross-set thicknesses can be analyzed quantitatively (Bridge and Best, 1997; Leclair et al., 1997; Jerolmack and Mohrig, 2005; Swanson et al., 2019; Cardenas et al., 2019). A primary metric used for such analysis is the coefficient of variation of cross-set thicknesses, c_v,

$$c_v = s_\sigma / s_m \qquad (1)$$

where s_m and s_σ are the mean and standard deviation of set thicknesses. The value of c_v for a given dune field is controlled by the ratio of dune migration rate to bed aggradation rate (Paola and Borgman, 1991; Bridge and Best, 1997; Leclair et al., 1997; Jerolmack and Mohrig, 2005; Cardenas et al., 2019). Dune heights are commonly gamma distributed, independent of setting -

i.e., fluvial, Paola and Borgman (1991); natural and experimental fluvial, van der Mark et al. (2008); experimental fluvial, Ganti et al., 2013; aeolian, Swanson et al. (2016). With gamma distributed dune heights, a dune field undergoing net bypass will have a set thickness c_v = 0.88 (± 0.03) (Paola and Borgman, 1991; Bridge, 1997; Jerolmack and Mohrig, 2005). The distribution of set thicknesses resulting from such a net bypass dune field will be exponentially distributed (Paola and Borgman, 1991; Jerolmack and Mohrig, 2005; Cardenas et al., 2019; Swanson et al., 2019). With a higher aggradation rate relative to the dune migration rate, the set thickness c_v will decrease until it reaches the coefficient of variation of the original bedform heights (Jerolmack and Mohrig, 2005) in the range of 0.29-0.60 (White Sands = 0.29, Swanson et al., 2016; Algodones = 0.45; Cardenas et al., 2019; fluvial dunes in the Trinity River = 0.60; Mason and Mohrig, in review). As the c_v decreases, the best-fit distribution of set thicknesses will also change to a gamma distribution. As the rate of bed aggradation approaches the rate of dune migration, this curve will also better represent the formative bedform heights (Jerolmack and Mohrig, 2005).

1.2 The Page and Entrada Sandstones, Earth

We use the Page and Entrada Sandstones, described below, as end-member aeolian dune-field strata, representing dry bypass (no water table; Page) and wet aggradation (water table; Entrada). The Jurassic middle middle Page Sandstone (hereafter, middle Page) is the record of at least six stacked aeolian dune fields, each in a state of near bypass (i.e., low sediment-accumulation rates/low aggradation) during which there was not a near-surface water table. Each bypass accumulation is separated from the others by formation-scale erosional surfaces (Havholm et al., 1993; Havholm and Kocurek, 1994; Blakey et al., 1996; Cardenas et al., 2019).

Episodic highstands in dune field water table, driven by highstands in the adjacent Carmel sea, helped preserve these bypass accumulations through subsidence sufficient for the strata to generally not be completely reworked during the following episode of aeolian sedimentation (Havholm et al., 1993; Blakey et al., 1996; Cardenas et al., 2019). The bypass state of the middle Page is recorded by the set thickness c_v of 0.90 and the exponential distribution of set thicknesses (Cardenas et al., 2019). Additionally, the distribution of dune heights has been reconstructed for the middle Page and can be reconstructed from any set of bypass strata with reasonable assumptions about the standard deviation of the population (Cardenas et al., 2019). In contrast with the Page, in the Entrada Sandstone, a rising near-surface water table drove significant aggradation even after antecedent topography was filled (Carr-Crabaugh et al., Kocurek and Day, 2018). This is represented by the set thickness c_v of 0.46, well within an aggradational limits and plausibly representing the cv of formative dune heights, as well as the gamma distribution of set thicknesses (Cardenas et al., 2019).

2. METHODS

We began with a population of field-acquired set thicknesses from the middle Page Sandstone (set thickness n = 402; data from Cardenas et al., 2019). The c_v of middle Page sets is 0.90 (Eq. 1; s_m = 2.44 m, s_σ = 2.20 m). The distribution is not rejected as exponential or gamma by a two-sample Kolmogorov-Smirnov tests comparing the distribution to randomly generated distributions of size n = 100 (Fig. 1). Both the c_v and the exponential distribution data are diagnostic of the bypass dynamics of the ancient Page dune fields. We tracked the change in these properties as we modified the distribution of set thicknesses to represent limitation imposed on the measurements by hypothetical measurement from remote sensing data.

This population of Page set thicknesses was modified by removing measurements below detectable thresholds in remote sensing images, and adding their thickness into adjacent sets. To do this, a value is calculated for each set called exposure distance, D_E, such that

$$D_E = s \, / \, tan\,(\theta). \qquad (2)$$

This represents the projection of the true vertical set thickness into a surface of dip θ in degrees from horizontal. For a given set thickness *s*, D_E increases as the outcrop dip θ approaches zero. That is, a set of *s* thickness is exposed across a longer horizontal distance D_E where the dip of the outcrop is shallower (Fig. 1). One thing to note is that *s,* as it is used in Eq. 2 and defined in Figure 1, is the apparent thickness of a set. In the experiments presented here, we assumed all strata are horizontal and so the apparent and true thicknesses are equal. If the strata are inclined at an angle Φ below the horizontal, Eq. 2 must be modified to use a true thickness that is different from the apparent thickness:

$$D_E = s_{TRUE}\, sin\,(\theta) \, / \, tan\,(\theta)\, cos\,(90 - \Phi - \theta). \qquad (2a)$$

With sufficient exposure, Φ can be measured using a DEM (e.g., Kite et al., 2016; Goudge et al., 2017; Hughes et al., 2019), in addition to the readily measured surface slope, θ. Equation 2 was run with a range from 1° to 60° at 1° intervals. Then, we defined a detection limit, D_L, such that

$$D_L = xR \qquad (3)$$

where *R* is the resolution of an image pixel (set here as the maximum resolution of HiRISE 0.25 m) and *x* is an assumed number of pixels required to identify a unique set. Although D_L shares units of distance with *R* for purposes of running the code, we will also refer to D_L as the associated number of pixels in the text. We set *x* to a range from 3 to 10 pixels at 1 pixel intervals, leading to D_L values of ranging from 0.75 m to 2.50 m at 0.25 m intervals. The length of three pixels is a typical rule of thumb for image detection limits, a reasonable lower bound to begin exploration of results. With 8 detection limits and 60 dips, 480 unique experiments were run.

Forty-five vertical sections composed of the thicknesses of stacked sets (Cardenas et al., 2019) were organized as columns in a matrix. For each section, the sets were tested for detection in order. For any given set, If $D_E \geq D_L$, that set that set was not modified. If $D_E < D_L$, then the set's thickness was added to adjacent sets depending upon its position, and then removed. If the first set was not detected, its thickness was added to the second. If the final set was not detected, its thickness was added to the previous set. If the set was between other sets, half of its thickness was added to the two adjacent sets. If the set was the only set in the section, it was labeled an automatic detection. One change was allowed to each section before another detection test was performed, until all sets passed the detection test. This process is analogous to the loss of sub-resolution data, as set thicknesses are blended together while overall section thickness is maintained. Finally, although HiRISE DEM resolution is four times coarser than visible images, this experiment assumed sub-pixel interpolations of elevation are reasonable so that DEM resolution would not be the limiting factor in the collection of set thickness measurements.

3. RESULTS

As outcrop dip (θ) increases, D_E for all sets decreases, dropping many sets below D_L. This leads to a decrease in the total number of sets, n, resulting from any experiment (Fig. 2). Note that because the thickness of each of the 45 vertical sections is preserved, a decrease in n is concurrent with a thickening of some sets. In the D_L = 3 pixels scenario, the first set is lost at θ = 13°, and the number of measurements n, drops as low as 249 (62% of original measurements) at 60° (Fig. 2). The loss of the first set occurs at only θ = 4° in the D_L = 10 pixels scenario, and n is reduced to only 66 sets (16% of original measurements) in the $\theta = 60°$ experiment. The loss of sets preferentially drives an underrepresentation of the thinner side of the distributions, represented by the shrinking of thinner histogram bars in Figure 3, as well as an increase in the mean set thickness. The loss of sets eventually leads to a significant reshaping of the distribution, seen clearly in the histograms (Fig. 3) and cumulative distribution functions (CDFs; Fig. 4) both as outcrop dip and detection limit increase. At any given detection limit, the loss of measurements and distribution reshaping occurs progressively from shallow to steeper surface dips (Figs. 3 and 4). In addition to the visual comparison, the similarity of the filtered dataset to the original is reported with a p-value produced by a two-sample Kolmogorov-Smirnov test. This is shown across the entire experimental domain in Figure 5, which contours the p-value results of all experiments at common critical p-values (0.001, 0.01, and 0.1).

The filtered histograms become increasingly gamma shaped with decreasing n, driven by the reduction in the thinnest end of the distribution, the increase in the mean and mode, and the thickening tails (Fig. 3). The comparison of the filtered datasets to the fitted distributions is more clearly made in the CDFs (Fig. 4). The progressive filtering and loss of sets reduces the quality of the exponential fit, seen visually and with p-values, but maintains and even increases the quality of the gamma fit (Fig. 4). The filtering also causes s_m to increase by as much as 610% in the most filtered dataset (Fig. 3L), while s_σ only increases by 249% (Figs. 3A vs 3L, and 6). The difference in sensitivity of these two parameters to the applied filtering has significant implications for c_v values (Eq. 1). The rapid increase in s_m relative to the slow increase in s_σ creates a steady decrease in c_v with decreasing n (Fig. 6). Figure 7 shows c_v as a function of the detection limit (D_L) for a number of outcrop dips (θ) ranging from 10° to 60°. These curves are compared to horizontal lines representing field measurements from the middle Page (Cardenas et al., 2019), and the Entrada (Crabaugh and Kocurek, 1993; Kocurek and Day, 2018). As D_L and θ increase, steeper outcrop dips deviate from Page values towards Entrada values, while shallow outcrop dips buffer the amount of data loss and change in c_v.

4. DISCUSSION

The results show that there is a significant risk of remote sensing cross-set thickness measurements not representing the actual stratigraphy, but also that there is a clear range of reasonable conditions for measurement of aeolian cross strata from HiRISE images (Fig. 5). Even at 10 pixel detection limits (Eq. 3), 10° dips (θ) do little to alter the original dataset, losing only up to the finest 4% of measurements (Figs. 2 and 3A-C). The preservation of measurements leads to the preservation of reconstructions of dune-field kinematics and dune heights, as the c_v of all filtered Page datasets at θ = 10° remain within bypass range (Fig. 7), consistent with interpretations of the original dataset (Cardenas et al., 2019; Swanson et al., 2019). A 30° dip is able to provide a meaningful measurement at a 3 pixel detection limit, with n = 96% of the original dataset (Figs. 3 and 7), but not beyond; at D_L = 4, the 30° dip moves beyond bypass (Fig. 7), only maintains n = 82% of the original data. This degree of blending has significantly altered the shape of the fitted distribution, leading to the rejection of an exponential fit (Figs. 4G and H). In terms of statistical similarity to the original dataset, only θ ≤ 13° can produce accurate measurements at all D_L (Fig. 5). Given the difficulty in truly knowing a detection limit, focusing on outcrops sloping ≤ 13°, or at least as shallowly as possible, is likely to result in the dataset most accurately representing the actual strata.

The effect of resolution filtering on Page dune field reconstructions becomes increasingly destructive with the increasing loss of thin sets. Much of this stems from the difference in response to the filtering by s_m and s_σ (Fig. 5). This indicates that the loss of data alters the shape of the fitted distribution, rather than simply translating it towards thicker measurements (Figs. 3 and 4). At worst, the low c_v values and the well-fit gamma curves would lead to the incorrect reconstruction of the middle Page dune fields as highly aggradational (Fig. 7), which would in turn lead to discussion regarding the environmental forcings driving aggradation instead of bypass (e.g., local topography, water table, changing wind regime; Kocurek and Day, 2018; Swanson et al., 2019; Cardenas et al., 2019). In the most filtered examples, the 30°, 45°, and 60° exposures have c_v values approaching that of parts of the Entrada sandstone (c_v = 0.46; Fig. 7), a wet, aggradational dune field which represents the end-member of aeolian dune field accumulation styles completely opposite to the dry bypass of the Page (Havholm et al., 1993; Crabaugh and Kocurek, 1993; Havholm and Kocurek, 1994). The reconstruction of the Page as an Entrada-type dune field represents the complete loss of an accurate dataset. Additionally, with a c_v well below 0.88, the ability to reconstruct the distribution of dune heights following the methodology of Cardenas et al. (2019) is lost.

Stack et al. (2013), in their Figure 14, show several examples of bed-thickness distributions from sedimentary outcrop on Mars. These distributions have shapes similar to our high-θ experimental results. Namely, exponential fits underestimate of the number of thin beds and overestimate of the number of thick beds (Fig. 3I-L). This is particularly apparent in several of their distributions measured in Holden crater, particularly those labeled H1, H3, H4-H8, and H10 in their Figure 14. Some of the local mean bed thicknesses in Holden crater reported in both Stack et al. (2013) and Day and Catling (2019) are within the D_L values tested here. Although these beds have distribution shapes similar to the filtered datasets reported here, it is not definitive enough to constrain whether or not these beds in Holden crater are aeolian cross sets, a hypothesis still being tested (Day and Catling, 2019).

The experiments performed here have additional implications for constraining the depositional environment of strata on Mars. Gamma and exponentially distributed cross set thicknesses, which should represent most aeolian cross sets, have been shown here to increase in mean set thickness (s_m) more rapidly than in standard deviation (s_σ) as filtering increases and the number of sets, n, decreases. This is not a characteristic shared by all distributions. Figure 8A shows the CDF of a normal distribution, generated randomly with n = 720, s_m = 2.98 m and s_σ = 1.02 m, such that it did not produce negative values and is in range to be modified by the previously used θ and D_L. Figure 8A compares this original distribution to the filtered distribution at θ = 60° and D_L = 6 pixels. The comparisons are qualitatively similar to the filtered Page datasets, and the p-values from a two-sample Kolmogorov-Smirnov test would similarly lead to rejection an exponential fit but do not reject a gamma fit (Fig. 4). A fit to a normal distribution is rejected as well using the same test ($p < 0.001$). The most distinctive departure of the normal distribution from the Page Sandstone results is that s_m and s_σ increase at a much more similar rate with decreasing n, leading to a c_v that starts low and increases with decreasing n (Figure 8B). By beginning with remote sensing set thicknesses rather than field measurements, this experiment could presumably be picked up somewhere at a middling n value to test the response of s_m, s_σ, and c_v to decreasing n. An increasing or steady c_v would then be diagnostic of an originally normal distribution, which would likely rule out aeolian origin, although a decreasing c_v pointing towards an original gamma or exponential distribution would not be unique to aeolian cross sets.

This method and these numerical experiments assume individual cross sets are uniform in thickness. This assumption is likely to be valid for dune accumulations in wet systems. However, in a dry aeolian system, during deposition, dune scour depth may vary, and thus cause set thickness to vary spatially. If such variation set thickness is present, the possible error associated with the presented workflow is correlated with both the magnitude of set thickness variability and the surface dip used to calculate the excursion distance. However, in this study, selected sections exhibited very low lateral variation in set thickness, which would be exaggerated for any outcrop dip less than vertical. Similarly, this method would be optimally applicable for either higher-dip exposures of cross sets, or regions with strata that approximate tabular cross sets. Future work is planned to explore the sensitivity of set thickness measurement to the three dimensionality of dune deposits with variable scour depths a numerical model, however, for large-scale dune cross sets, this effect is hypothesized to be minimal.

5. CONCLUSION

As a community, we are in a good technological position to significantly improve our understanding of Mars' aeolian history, as aeolian deposits are far more likely to have bed thicknesses measurable with remote observations than fluvial or submarine strata. An understanding of the sedimentology down to the scale of individual beds, regardless of depositional setting, is fundamental to paleo-environmental reconstructions. The results of the numerical experiment conducted here are specific to the Page Sandstone, but offer a general framework to address problems surrounding the finite size of pixels in remotely collected raster images and irregular outcrop topography when measuring strata thicknesses on Mars. Where possible, measurements should be made from shallow-sloping (≤ 13°) outcrops, such that thin sets are fully represented because they are exposed over long distances. The experiments here may also prove useful in reconstructing the original distribution of sets by testing the response of a remotely measured dataset to further filtering. Finally, with many considering that aeolian strata may compose more of Mars' rock record than previously recognized (e.g., Anderson et al., 2018; Day and Catling, 2019), this work provides strong quantitative tools with which to interpret these strata and to understand possible sources of error.

6. ACKNOWLEDGEMENTS

The work presented here has improved following discussions with Katie Stack Morgan. BTC acknowledges support from the RioMar industry consortium and a University of Texas Graduate School fellowship. Set-thickness distributions are available at Caltech's Research Data Repository (https://data.caltech.edu/records/1277).

7. REFERENCES

Allen, J.R.L. (1973) A classification of climbing-ripple cross-lamination. Journal of the Geological Society, 129, 537-541.

Anderson, R.B., Edgar, L.A., Rubin, D.M., Lewis, K.W., and Newman, C. (2018) Complex bedding geometry in the upper portion of Aeolis Mons, Gale Crater, Mars. Icarus, 314, 246-264.

Banham, S.G., Gupta, S., Rubin, D.M., Watkins, J.A., Sumner, D.Y., Edgett, K.S., Grotzinger, J.P., Lewis, K.W., Edgar, L.A., Stack-Morgan, K.M., Barnes, R., Bell III, J.F., Day, M.D., Ewing, R.C., Lapotre, M.G.A., Stein, N.T., Rivera-Hernandez, F., and Vasavada, A.R. (2018) Ancient Martian aeolian processes and palaeomorphology reconstructed from the Stimson formation on the lower slope of Aeolis Mons, Gale crater, Mars. Sedimentology, 65, 993-1042.

Blakey, R.C., Havholm, K.G., and Jones, L.S. (1996) Stratigraphic analysis of eolian interactions with marine and fluvial deposits, Middle Jurassic Page Sandstone and Carmel Formation, Colorado Plateau, USA. Journal of Sedimentary Research, 66, 324-342.

Bramble, M.S., Goudge, T.A., Milliken, R.E., and Mustard, J.F. (2019) Testing the deltaic origin of fan deposits at Bradbury Crater, Mars. Icarus, 319, 363-366.

Bridge, J. (1997) Thickness of sets of cross strata and planar strata as a function of formative bed-wave geometry and migration, and aggradation rate. Geology, 25, 971-974.

Bridge, J., and Best, J. (1997) Preservation of planar laminae due to migration of low-relief bed waves over aggrading upper-stage plane beds: comparison of experimental data with theory. Sedimentology, 44, 253–262.

Cardenas, B.T., Kocurek, G., Mohrig, D., Swanson, T., Hughes, C.M., and Brothers, S.C. (2019) Autogenic processes and allogenic forcings preserved in set-scale aeolian stratigraphy II: the scour-and-fill dominated Jurassic Page Sandstone, Arizona, USA. Journal of Sedimentary Research, v. 89, p. 741-760.

Chojnacki, M., Banks, M.E., Fenton, L.K., and Urso, A.C. (2019) Boundary condition controls on the high-sand-flux regions of Mars. Geology, 47, 427-430.

Chojnacki, M., Johnson, J.R., Moersch, J.E., Fenton, L.K., Michaels, T.I., and Bell III, J.F. (2015) Persistent aeolian activity at Endeavour crater, Meridiani Planum, Mars: new observations from orbit and the surface. Icarus, 251, 275-290.

Cornwall, C., Bourke, M.C., Jackson, D.W.T., and Cooper, J.A.G. (2018a) Aeolian slipface dynamics and grainflow morphologies on Earth and Mars. Icarus, 314, 311-326.

Cornwall, C., Jackson, D.W.T., Bourke, M.C., and Cooper, J.A.G. (2018b) Morphometric analysis of slipface processes of an aeolian dune: Implications for grain-flow dynamics. Sedimentology, 65, 2034-2054.

Crabaugh, M., and Kocurek, G. (1993) Entrada Sandstone: an example of a wet aeolian system, in Pye, K., ed., The Dynamics and Environmental Context of Aeolian Sedimentary Systems: Geological Society of London, Special Publications 72, 103–126.

Day, M.D., and Catling, D.C. (2018) Dune casts preserved by partial burial: The first identification of ghost dune pits on Mars. Journal of Geophysical Research: Planets, 123, 1431-1448.

Day, M.D., and Catling, D.C. (2019) Potential aeolian deposition of intra-crater layering: A case study of Henry crater, Mars. Geological Society of America Bulletin, in press.

Day, M.D., and Kocurek, G. (2016) Observations of an aeolian landscape: From surface to orbit in Gale crater. Icarus, 280, 37-71.

Day, M.D., and Kocurek, G. (2018) Pattern similarity across planetary dune fields. Geology, 46, 999-1002.

Ewing, R.C., and Kocurek, G. (2010a) Aeolian dune-field pattern boundary conditions. Geomorphology, 114, 175–187.

Ewing, R.C., and Kocurek, G. (2010b) Aeolian dune interactions and dune-field pattern formation: White Sands Dune Field, New Mexico. Sedimentology, 57, 1199-1219.

Ewing, R.C., Peyret, A.-P.B., Kocurek, G., and Bourke, M. (2010) Dune field pattern formation and recent transporting winds in the Olympia Undae Dune Field, north polar region of Mars: Journal of Geophysical Research: Planets. 115, E08005.

Fenton, L.K., and Hayward, R.K. (2010) Southern high latitude dune fields on Mars: Morphology, aeolian inactivity, and climate change. Geomorphology, 121, 98-121.

Ganti, V., Paola, C., and Foufoula-Georgiou, E. (2013) Kinematic controls on the geometry of the preserved cross sets. Journal of Geophysical Research: Earth Surface, 118, 1296-1307.

Goudge, T.A., Milliken, R.E., Head, J.W., Mustard, J.F., and Fassett, C.I., 2017, Sedimentological evidence for a deltaic origin of the western fan deposit in Jezero craters, Mars and implications for future exploration. Earth and Planetary Science Letters, 458, 357-365.

Grotzinger, J.P., Arvidson, R.E., Bell III, J.F., Calvin, W., Clark, B.C., Fike, D.A., Golombek, M., Greeley, R., Haldemann, A., Herkenhoff, K.E., Jolliff, B.L., Knoll, A.H., Malin, M., McLennan, S.M., Parker, T., Soderblom, L., Sohl-Dickstein, J.N., Squyres, S.W., Tosca, N.J., and Watters, W.A. (2005) Stratigraphy and sedimentology of a dry to wet eolian depositional system, Burns formation, Meridiani Planum, Mars. Earth and Planetary Science Letters, v. 240, p. 11-72.

Grotzinger, J.P., and Milliken, R.E. (2012) The sedimentary rock record of Mars: Distribution, origins, and global stratigraphy. in eds. Grotzinger, J.P., and Milliken, R.E., Sedimentary Geology of Mars, SEPM Special Publication 102, 1-48.

Havholm, K.G., and Kocurek, G. (1994) Factors controlling aeolian sequence stratigraphy: clues from super bounding surface features in the Middle Jurassic Page Sandstone. Sedimentology, 41, 913-934.

Havholm, K.G., Blakey, R.C., Capps, M., Jones, L.S., King, D.D., and Kocurek, G. (1993) Aeolian genetic stratigraphy: an example from the Middle Jurassic Page sandstone, Colorado Plateau. in Pye, K., and Lancaster, N., eds., Aeolian Sediments: Ancient and Modern. International Association of Sedimentologists Special Publication 16, 87–107.

Jerolmack, D.J., and Mohrig, D. (2005) Frozen dynamics of migrating bedforms. Geology, 33, 57–60.

Kirk, R.L., Howington-Kraus, E., Rosiek, M.R., Anderson, J.A., Archinal, B.A., Becker, K.J., Cook, D.A., Galuszka, D.M., Geissler, P.E., Hare, T.M., Holmberg, I.M., Keszthelyi, L.P., Redding, B.L., Delamere, W.A., Gallagher, D., Chapel, J.D., Eliason, E.M., King, R., and McEwen, A.S. (2008) Ultrahigh resolution topographic mapping of Mars with MRO HiRISE stereo images: Meter-scale slopes of candidate Phoenix landing sites. Journal of Geophysical Research: Planets, 113, E00A24.

Kite, E.S., Lewis, K.W., Lamb, M.P., Newman, C.E., and Richardson, M.I. (2013) Growth and form of the mound in Gale Crater, Mars: Slope wind enhanced erosion and transport. Geology, 41, 543-546.

Kite, E.S., Sneed, J., Mayer, D.P., Lewis, K.W., Michaels, T.I., Hore, A., and Rafkin, S.C.R. (2016) Evolution of major sedimentary mounds on Mars: Buildup via anticompensational stacking modulated by climate change. Journal of Geophysical Research: Planets, 121, 2282-2324.

Kocurek, G., and Day, M.D. (2018) What is preserved in the aeolian rock record? A Jurassic Entrada Sandstone case study at the Utah–Arizona border. Sedimentology, 65, 1301-1321.

Kocurek, G., Ewing, R.C., and Mohrig, D. (2010) How do bedform patterns arise? New views on the role of bedform interactions within a set of boundary conditions. Earth Surface Processes and Landforms, 35, 51–63.

Lapotre, M.G.A., Ewing, R.C., Lamb, M.P., Fischer, W.W., Grotzinger, J.P., Rubin, D.M., Lewis, K.W., Ballard, M.J., Day, M., Gupta, S., Banham, S.G., Bridges, N.T., Des Marais, D.J., Fraeman, A.A., Grant, J.A., Herkenhoff, K.E., Ming, D.W., Mischna, M.A., Rice, M.S., Sumner, D.Y., Vasavada, A.R., and Yingst, R.A. (2016) Large wind ripples on Mars: A record of atmospheric evolution. Science, 353, 55-58.

Leclair, S.F., Bridge, J.S., and Wang, F. (1997) Preservation of cross-strata due to migration of subaqueous dunes over aggrading and non-aggrading beds: comparison of experimental data with theory. Geoscience Canada, 24, 55-66.

Lewis, K.W., Aharonson, O., Grotzinger, J.P., Squyres, S.W., Bell III, J.F., Crumpler, L.S., and Schmidt, M.E. (2008a) Structure and stratigraphy of Home Plate from the Spirit Mars Exploration Rover. Journal of Geophysical Research, 113, E12S36.

Lewis, K.W., Aharonson, O., Grotzinger, J.P., Kirk, R.L., McEwen, A.S., and Suer, T.-A. (2008b) Quasi-periodic bedding in the sedimentary rock record of Mars. Science, 322, 1532-1535.

Mason, J., and Mohrig, D., in review, Bedform groups during flood on the Trinity River – a new scale of self-organization in river bottom topography.

McEwen, A.S., Eliason, E.M., Bergstrom, J.W., Bridges, N.T., Hansen, C.J., Delamere, W.A., Grant, J.A., Gulick, V.C., Herkenhoff, K.E., Keszthelyi, L., Kirk, R.L., Mellon, M.T., Squyres, S.W., Thomas, N., and Weitz, C.M. (2007) Mars Reconnaissance Orbiter's High Resolution Imaging Science Experiment (HiRISE). Journal of Geophysical Research: Planets, 112, E05202.

Milliken, R.E., Ewing, R.C., Fischer, W.W., and Hurowitz, J. (2014) Wind-blown sandstones cemented by sulfate and clay minerals in Gale Crater, Mars. Geophysical Research Letters, 41, 1149-1154.

Paola, C., and Borgman, L. (1991) Reconstructing random topography from preserved stratification. Sedimentology, 38, 553–565.

Pipiringos, G.N., and O'Sullivan, R.B. (1978) Principal unconformities in Triassic and Jurassic rocks, western interior United States; a preliminary survey. United States Geologic Survey, Professional Paper, 1035–A, 35 p.

Rubin, D.M., and Hunter, R.E. (1982) Bedform climbing in theory and nature. Sedimentology, 29, 121-138.

Silvestro, S., Vaz, D.A., Ewing, R.C., Rossi, A.P., Fenton, L.K., Michaels, T.I., Flahaut, J., and Geissler, P.E. (2013) Pervasive aeolian activity along rover Curiosity's traverse in Gale Crater, Mars. Geology, 41, 483-486.

Silvestro, S., Vaz, D.A., Fenton, L.K., and Geissler, P.E. (2011) Active aeolian processes on Mars: A regional study in Arabia and Meridiani Terrae. Geophysical Research Letters, 38, L20201.

Swanson, T., Mohrig, D., Kocurek, G., Cardenas, B.T., and Wolinsky, M.A. (2019) Autogenic processes and allogenic forcings preserved in set-scale aeolian stratigraphy I: Numerical experiments. Journal of Sedimentary Research, v. 89, p. 728-740.

Swanson, T., Mohrig, D., & Kocurek, G. (2016). Aeolian dune sediment flux variability over an annual cycle of wind. Sedimentology, 63, 1753–1764.

van der Mark, C.F., Blom, A., and Hulscher, S.J.M.H. (2008) Quantification of variability in bedform geometry. Journal of Geophysical Research, 113, F03020.

8. FIGURES AND CAPTIONS

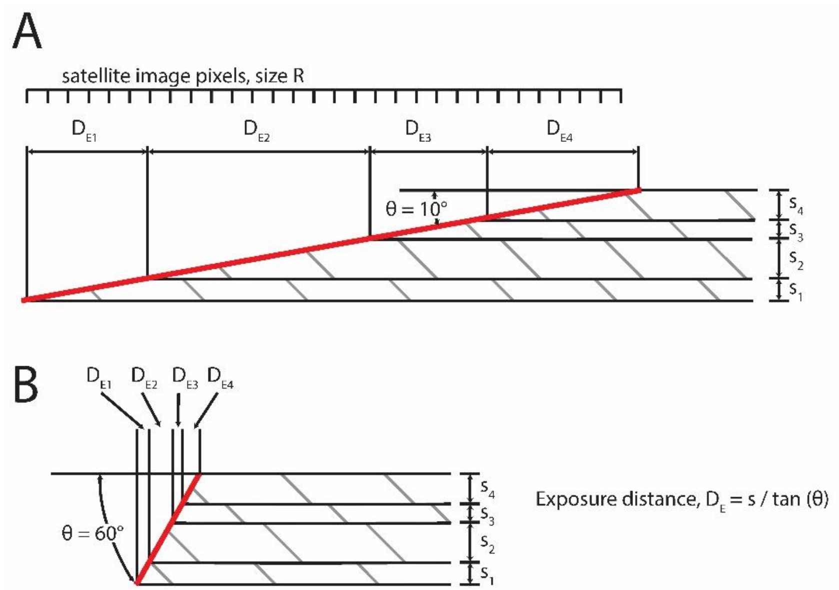

Figure 1 – A: Experiment schematic showing why exposure distance, D_E, is a function of outcrop dip (red surface, $\theta = 10°$) and cross-set thickness, s. Satellite resolution, R, is shown in relation to D_E. B: An increased outcrop dip ($\theta = 60°$) results in decreased D_E for the same s values as panel A. The formula to calculate D_L and D_E are shown, assuming horizontal strata.

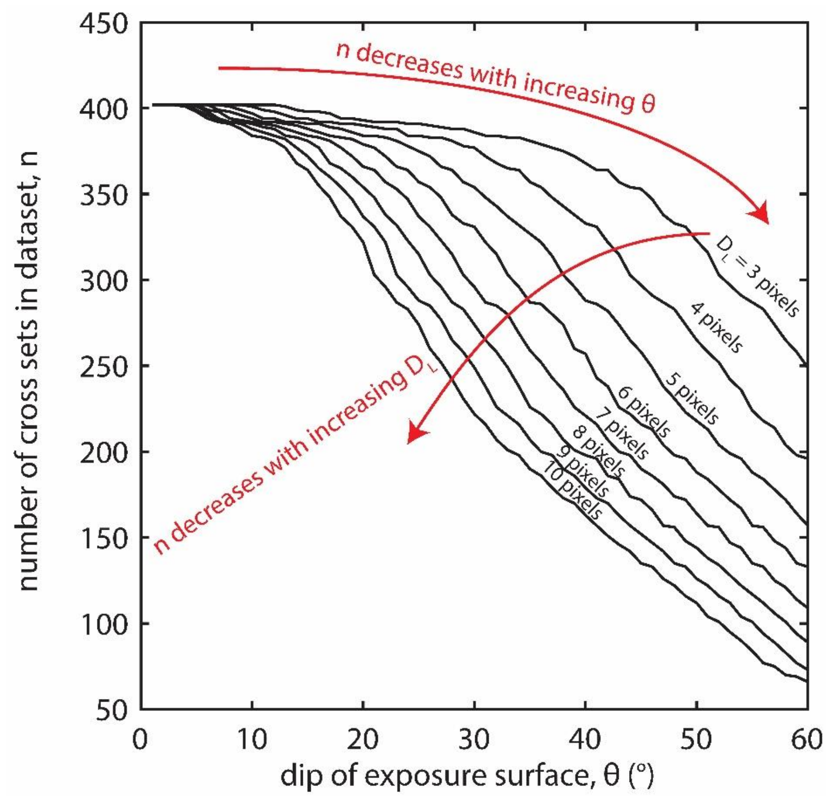

Figure 2 – The effect of blending sets (Fig. 1) on the number of sets in the filtered dataset, as a function of the dip of the exposure surface (θ) and the detection limit (D_L). The number of sets (n), and thus the degree of change from the original dataset, is largely controlled by θ, which also amplifies the effect of D_L at high θ. Wiggles in the lines are due to the threshold nature of the resolution-based set length filtering.

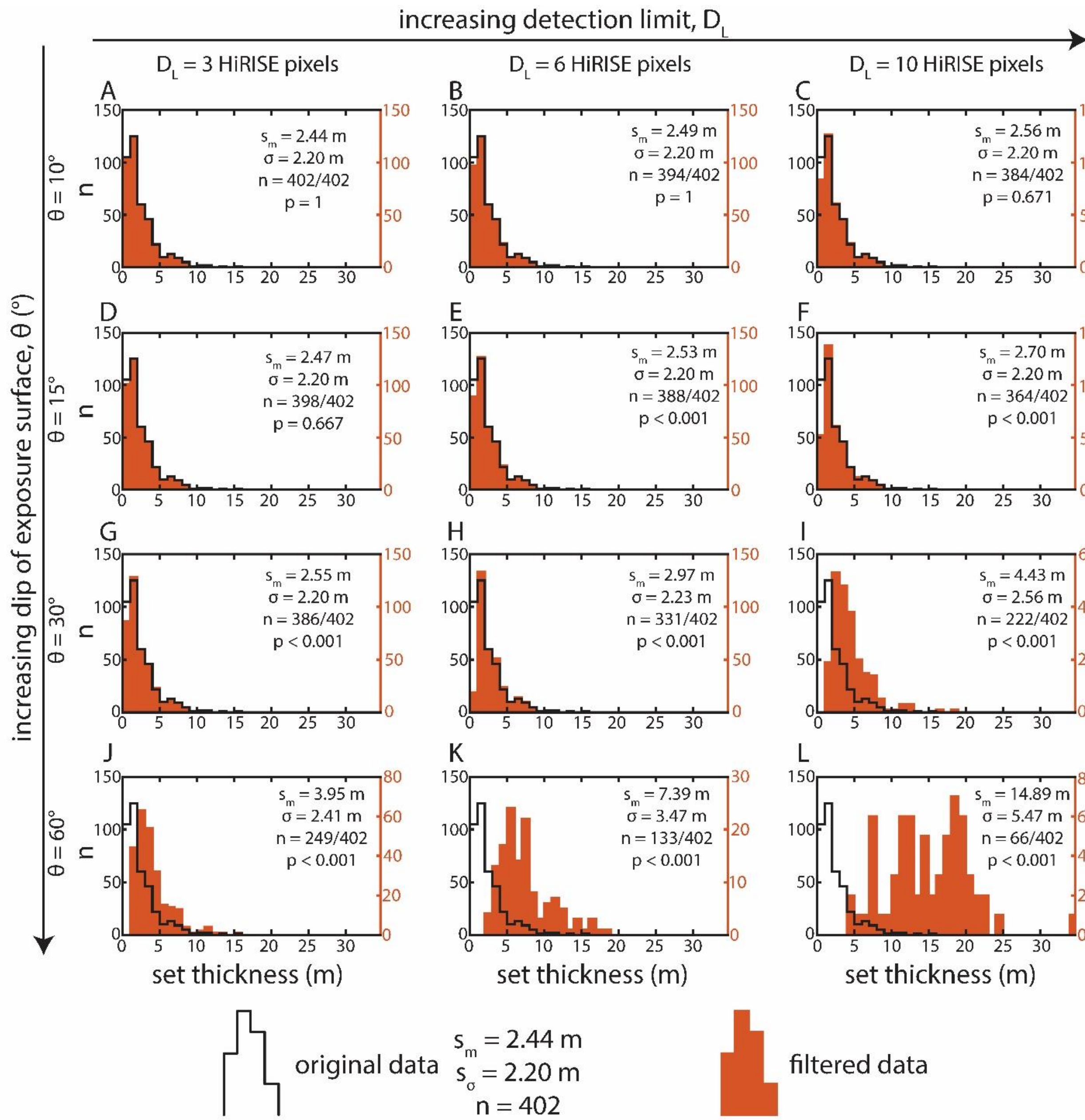

Figure 3 – A-L: Histograms comparing the original distribution of Page set thicknesses (black line) to 12 filtered distributions (red filled). All histograms have two y axes showing n for the original data (left) and filtered data (right), and 1 m bins. The filtering of thin sets is performed as a function of outcrop dip and assumed detection limits (Fig. 1). Each panel shows the filtered data's mean, standard deviation, n, and p-value in comparison to the original dataset, calculated using a two-sample Kolmogorov-Smirnov test. Columns represent experimental results at

detection limits (D_L) = 3, 6, and 10 HiRISE pixels. Rows represents results at exposure dips (θ) of 10°, 15°, 30°, and 60°. In general, increases in D_L and θ create filtered datasets of decreasing similarity to the original, both in terms of shape, statistical moments, and number of measurements.

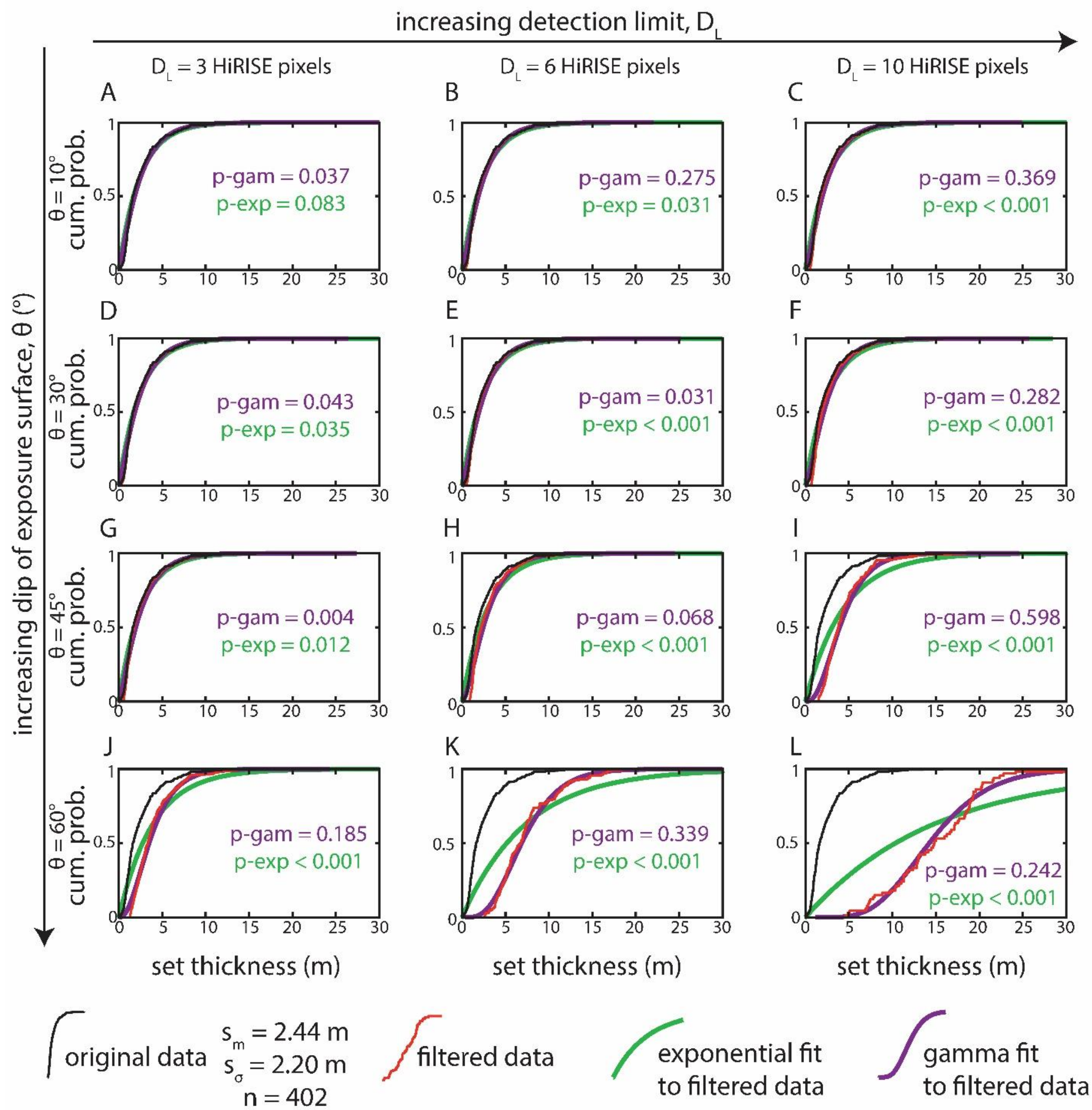

Figure 4 – A-L: Cumulative distribution functions (CDFs) comparing filtered data to fitted exponential and gamma curves, as well as the original dataset (each panel shows the same data shown in Fig. 2). The filtering of sets was performed as a function of outcrop dip and assumed detection limits (Fig. 1). Shown in these panels are the p-values from the two-sample Kolmogorov-Smirnov test of similarity between the filtered data and the fitted gamma and exponential distributions. The filtered data's mean, standard deviation, and n values are shown in

the associated panels of Figure 2. Columns represent experimental results at detection limits (D_L) = 3, 6, and 10 HiRISE pixels. Rows represents results at exposure dips (θ) of 10°, 15°, 30°, and 60°. The progressive filtering of sets coincides with the continued departure from the statistical moments of the original data, as well as the change in shape to gamma distributed, which was maintained in all the experiments.

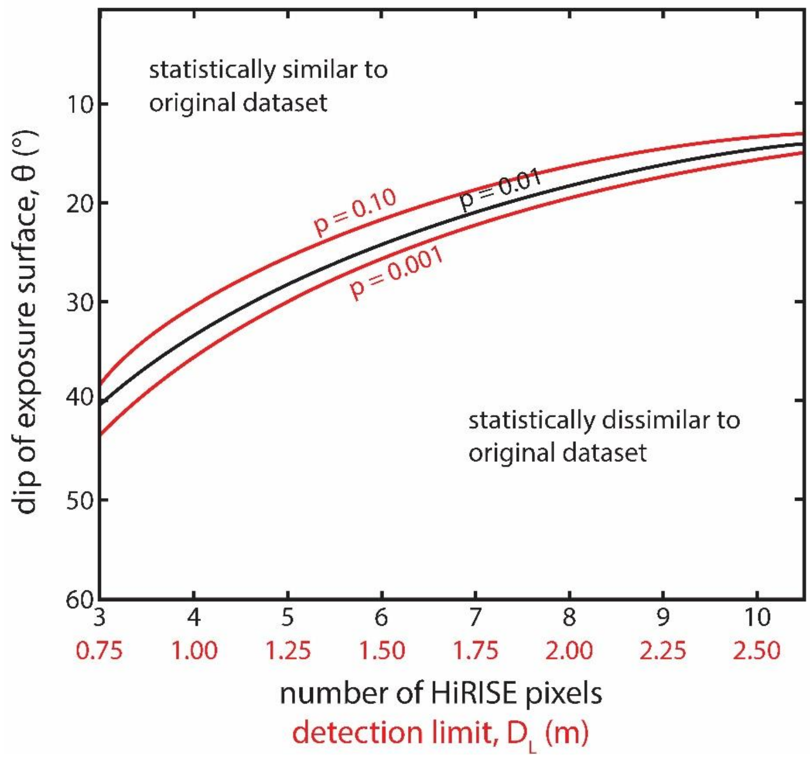

Figure 5 – The detection limit (D_L) and the dip of the exposure surface (θ) as controls on the statistical similarity of filtered datasets to the original. The red and black lines are contours at p-values of 0.10, 0.01, and 0.001 calculated from a two-sample Kolmogorov-Smirnov test. These p-values are commonly used as critical p-values for rejecting the similarity of two datasets or not.

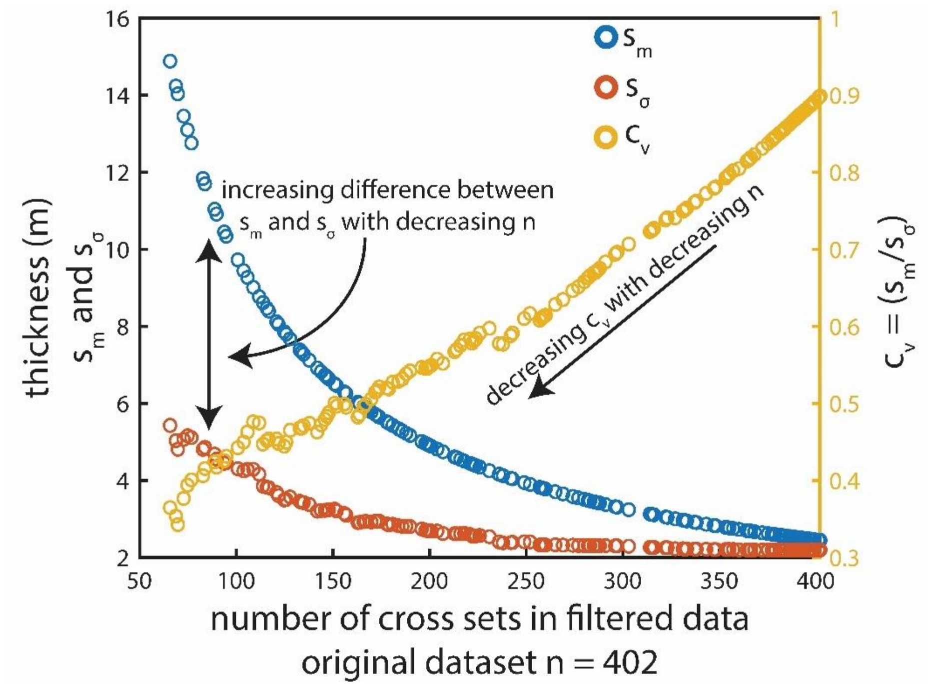

Figure 6 – Change in mean set thickness (s_m), standard deviation of set thickness (s_σ), and coefficient of variation of set thickness ($c_v = s_m / s_\sigma$) as a function of the number of cross sets (n) in the filtered datasets. As n decreases with increased filtering, s_m increases more rapidly than s_σ, causing a drop in c_v. The c_v is an important value for reconstructing the history of aeolian dune fields from preserved cross sets, and the change in c_v seen over this plot is significant enough to alter that reconstruction.

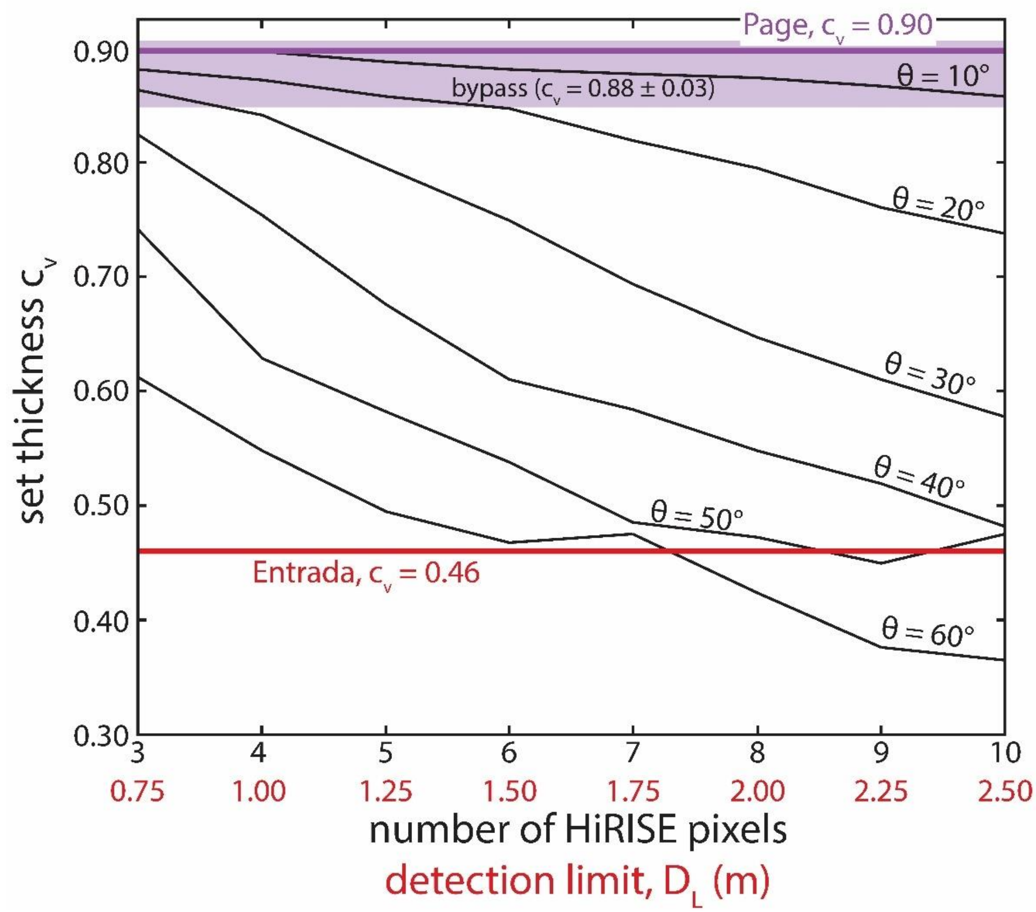

Figure 7 – The detection limit, D_L (Eq. 2), vs. the coefficient of variation, c_v (Eq. 1), of filtered and original datasets. The c_v of the unfiltered Page and Entrada data (Kocurek and Day, 2018; Cardenas et al., 2019) are shown with bold colored lines. A range of c_v values representing bypass is shown in the purple area (0.88 ± 0.03; Paola and Borgman, 1991; Bridge, 1997). Lower *cv* values are increasingly interpreted as aggradational dune fields (Bridge and Best, 1997; Jerolmack and Mohrig, 2005). The Page and Entrada represent opposite types of dune field accumulations (dry and bypassing vs. wet and aggrading). This is represented by their different c_v values. Black lines represent the c_v of the filtered Page datasets at different outcrop dips (θ) and D_L values. Increasing detection limits decrease the filtered c_v only slightly at θ = 10°, and in fact does not leave the range of bypass. The effect is more significant at all higher dips. The c_v of θ = 20° and 30° are within the range of bypass at D_L = 3 and 5 pixels, but move beyond bypass

range at higher D_L. At θ = 40° to 60°, c_v values are lower than bypass, even at D_L = 3 pixels. The c_v of θ = 50° and 60° is equal to or less than the Entrada c_v at D_L = 8 and 9 pixels, representing the complete loss of data quality which would lead to the end-member misinterpretation of the Page accumulation history.

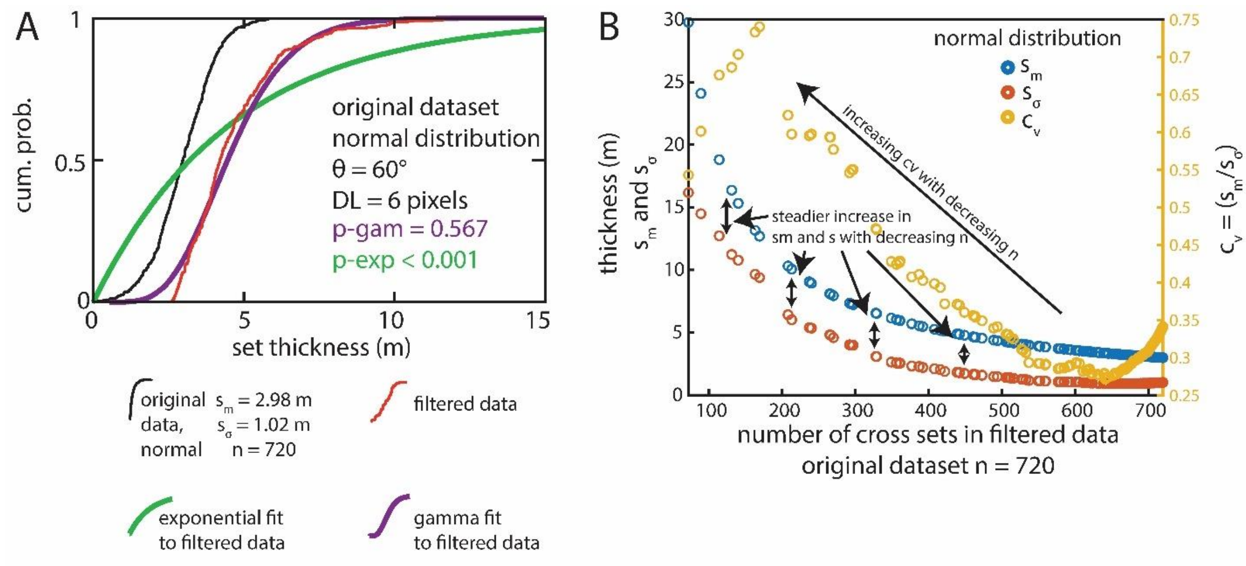

Figure 8 – A normal distribution of cross sets run through the same experiments as the Page sets, with the intention of looking for unique responses to the filtering process. A: CDF plot comparing the original normal dataset to a filtered dataset and the filtered dataset's fitted exponential and gamma distributions. P values are shown for the fits to the filtered data. Similar to the Page sets, filtering produces a dataset that is gamma shaped rather than exponential. B: Plot comparing the mean set thickness (s_m), standard deviation of set thickness (s_σ), and coefficient of variation of set thickness ($c_v = s_m / s_\sigma$) of the normal distribution in panel A as functions of the number of sets in an experiment, *n*. Unlike the exponentially distributed Page sets (Fig. 6), the normal sets show a steady increase in both s_m and s_σ, which creates a steady increase in c_v.